Chapter 4

Geometry of structures of a passive scalar fluctuation field in stationary isotropic homogeneous turbulence

4.1 DNS database

We use a numerical database obtained from a DNS with 512^3 grid points; the incompressible Navier–Stokes equations for the velocity field and the advection–diffusion equation for the passive scalar fluctuation were solved by means of a Fourier-Galerkin pseudo-spectral method. The domain is a cube of side 2π with periodic boundary conditions. The velocity field was forced at large scales, becoming statistically stationary in time. A mean scalar gradient was imposed so that the scalar fluctuation field became also statistically stationary in time. Despite the mean scalar gradient applied, the scalar fluctuation is statistically homogeneous. The Reynolds number based on the integral length scale is 1901, whereas the Taylor Reynolds number is $Re_\lambda = 265$. The Schmidt number of the simulation is $Sc = 0.7$. The product of the largest dynamically significant wavenumber, $k_{\max}$, and the average Kolmogorov length scale, $\bar\eta$, is $k_{\max}\eta = 1.05$. More specific details of the database can be found in O'Gorman & Pullin (2004).
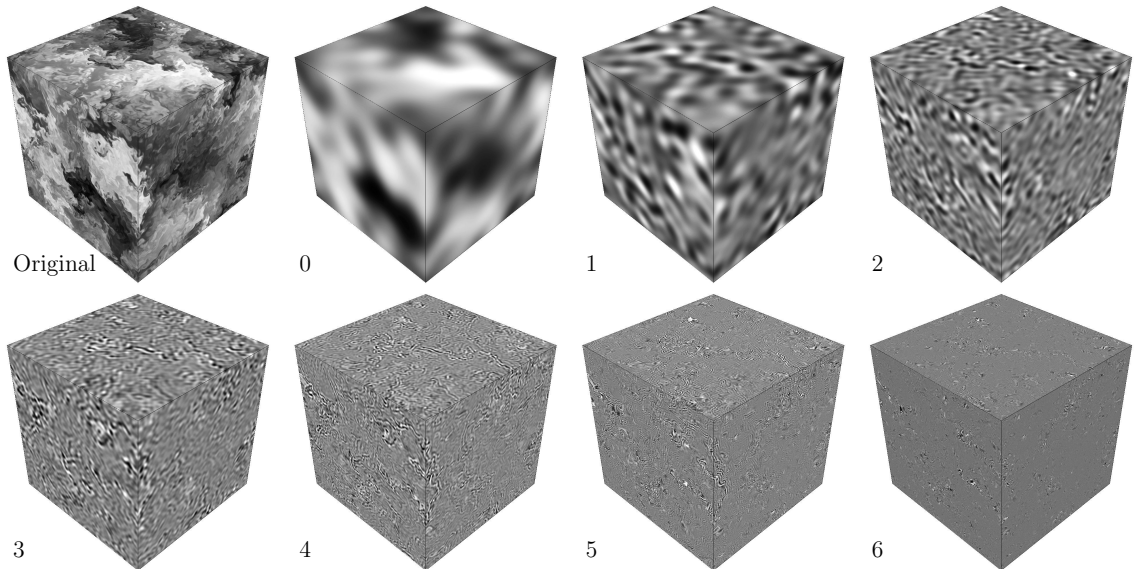
Figure 4.1: Tri-plane cuts of the passive scalar fluctuation field for the original database (top left) and each of the filtered scales resulting from the multi-scale analysis (filtering in curvelet domain) (increasing scale number from left to right and top to bottom)

4.2 Multi-scale diagnostics

We apply our methodology to the three-dimensional scalar field given by the passive scalar fluctuation at an instant in time. For the given resolution of 512^3 grid points, and a coarsest scale $j_0 = 2$, the curvelet transform provides seven scales. They will be named by a scale number, from 0 to 6; increasing values of the scale number correspond to smaller scales. Thus, scale 0 captures the largest scales and 6 the smallest. Figures 4.1 and 4.2 show the result of the multi-scale analysis based on the curvelet transform. Plane cuts of the original database and each of the filtered scales (filtered in the curvelet domain and then inverse transformed to the physical domain) are shown. Three-dimensional views with plane cuts in the three directions of the volume data are presented in Figure 4.1, and more detailed plane cuts normal to the x_3-direction at half the length of the cube are shown in Figure 4.2. Volume-data pdfs obtained for the scalar field associated with the original database and for each one of the filtered scales, Figure 4.3(a), give insight into the distribution of the scalar values at the different scales and their contribution to the total field (original database). For this scalar field, the pdfs tend to become narrower for increasing values of the scale number, that is, for smaller scales. Scalar fluctuation spectra are also computed for the original volume data
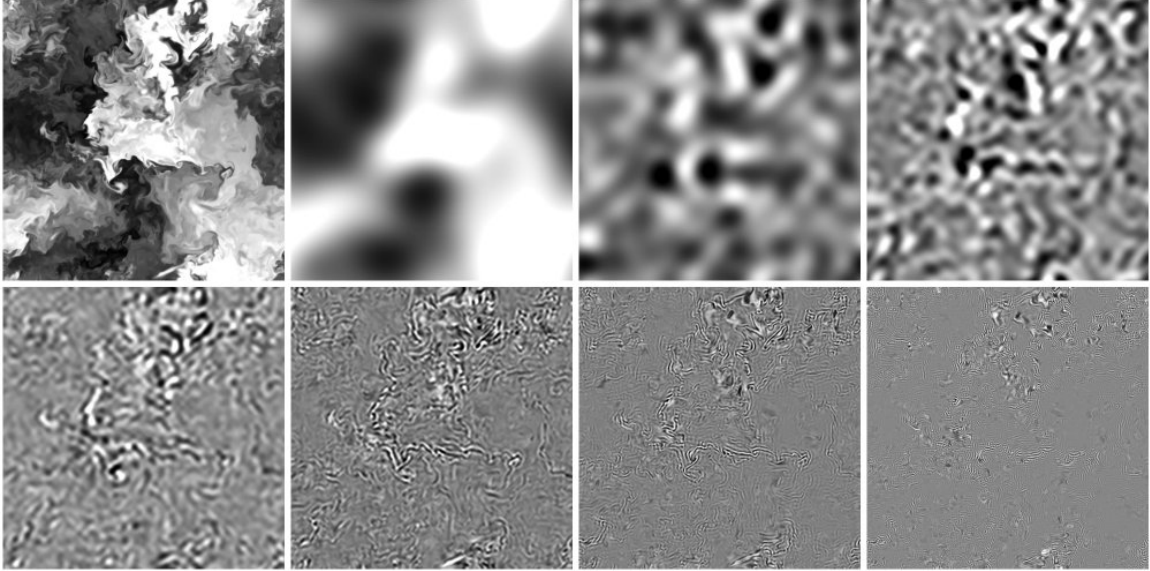
Figure 4.2: Plane cuts normal to the x_3-axis at its midpoint of the passive scalar fluctuation field for the original database (top left) and each one of the filtered scales resulting from the multi-scale analysis (filtering in curvelet domain) (increasing scale number from left to right and top to bottom)
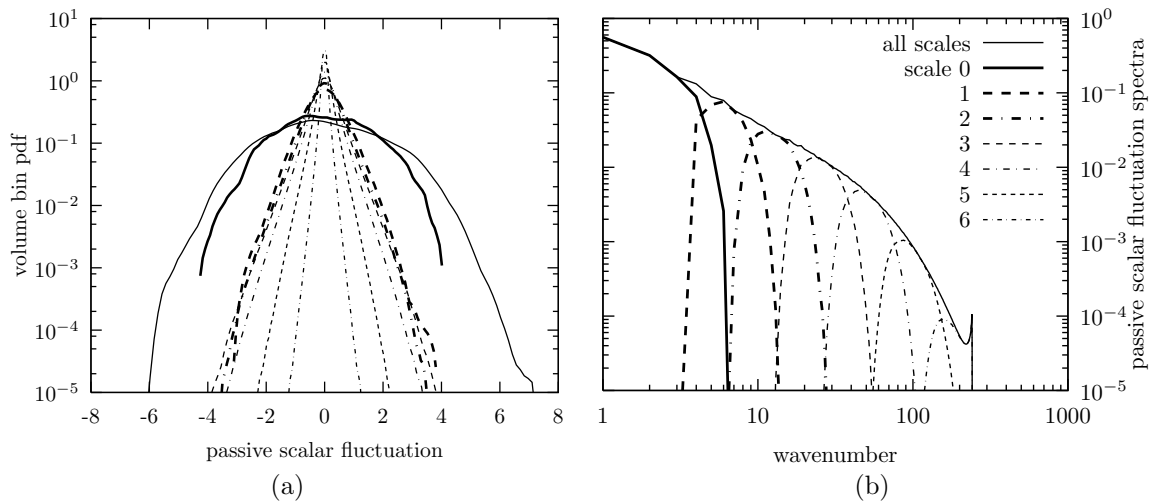
Figure 4.3: Volume-data pdfs of the passive scalar fluctuation field (a) and corresponding spectra (b), associated with the original database (containing all scales) and each of the filtered scales

field and each filtered scale and are shown in Figure 4.3(b). The effect of the curvelet filtering in the Fourier domain can be observed. This differs from a top-hat window filtering in that domain, in order to preserve the localization in the physical domain. It can be noticed that scales 1, 2, and 3 correspond mainly to the inertial range of scales, whereas scales 4 and 5 are mainly dissipation scales. From this observation and from Figure 4.3(a) we note that those pdfs associated with the scales corresponding to the inertial range (1, 2 and 3) are very similar, almost collapsing in that

plot.

Additionally, an equivalent multi-scale decomposition is done for the velocity field. That allows us to define characteristic squared integral velocities, $\overline{u_i^2}$, and integral length scales, L_i, L_i', for each filtered scale, i, in the same terms in which they are defined for the original velocity field. For the case of isotropic turbulence, they can be expressed as

$$\overline{u_i^2} = \frac{2}{3} \int_0^\infty E_i(k)\mathrm{d}k, \tag{4.1}$$

$$L_i = \frac{\pi}{2\overline{u^2}} \int_0^\infty \frac{E_i(k)}{k}\mathrm{d}k, \tag{4.2}$$

$$L_i' = \frac{\pi}{2\overline{u_i^2}} \int_0^\infty \frac{E_i(k)}{k}\mathrm{d}k, \tag{4.3}$$

where $E_i(k)$ is the energy spectrum associated with scale i, and the absence of subindex refers to the original velocity field. It follows from equation 2.5 that the sums of the energy spectra and the characteristic squared integral velocities of all the filtered scales is equal to those of the original velocity field, $E(k)$ and $\overline{u^2}$, respectively:

$$E(k) = \sum_i E_i(k), \tag{4.4}$$

$$\overline{u^2} = \sum_i \overline{u_i^2}. \tag{4.5}$$

Table 4.1 shows, for the original velocity field and for each filtered scale, the characteristic squared integral velocity and the characteristic integral length scale, and how they compare to the total characteristic squared integral velocity, $\overline{u^2}$, and the average Kolmogorov length scale, $\bar{\eta}$.

4.3 Geometry of passive scalar iso-surfaces

After the multi-scale analysis, iso-surfaces are obtained for each of the filtered scales. The contour values are, for each filtered scale, the mean value of the scalar field plus two times the standard deviation of that field (mean and standard deviation values can be obtained from the first- and

scale	$\overline{u_i^2}/\overline{u^2}$	$L_i/\bar{\eta}$	$L_i'/\bar{\eta}$
original	1.000	249.6	249.6
0	0.591	226.9	383.8
1	0.155	14.68	96.1
2	0.113	5.235	46.2
3	0.085	1.927	22.8
4	0.044	0.519	11.9
5	0.011	0.070	6.3
6	0.001	0.004	3.3

Table 4.1: Breakdown of characteristic integral velocities and length scales for the filtered scales

second-order moments of the volume pdfs presented before) (see Figure 4.4). Those iso-surfaces corresponding to the same relative contour value at each scale will be characterized and classified and their results compared among the different scales. We also remark that an additional step in the extraction is applied to periodically reconnect those structures intersecting boundaries with their continuation on the opposite boundaries; this reconnection is performed for each individual filtered scale. Both the largest scale (0) and the smallest scale (6) are not considered in the process: the largest scale is of less relevance in this analysis since its structure is expected to depend on the boundary conditions and external forces applied. The smallest scale is excluded to avoid the extraction of spurious structures and/or an erroneous geometrical characterization that could result from the lack of grid resolution, or aliasing effects at that scale. Thus, the scale numbers under analysis are 1–5. In the same spirit, a minimum number of points (300) was considered for a structure to be analyzed, so that it is smooth enough for a reliable calculation of its differential-geometry properties, the basis of the characterization step.

Then, each structure is geometrically characterized as described in §2.2 and, based on the parameters extracted from its signature, it can be represented in the visualization space referred in §2.3. Figures 4.5 and 4.6 show the distribution of glyphs representing each structure, for the different scale numbers 1–5 considered. In this case, glyphs are spheres whose centers correspond to the $\hat{S}, \hat{C}, \lambda$ parameters and whose radii are scaled according to the surface area of the structure, and their color is assigned based on the scale number to which the structure belongs. First, structures of all scales are shown and then the progression for individual scales is presented. As can be seen, the structures
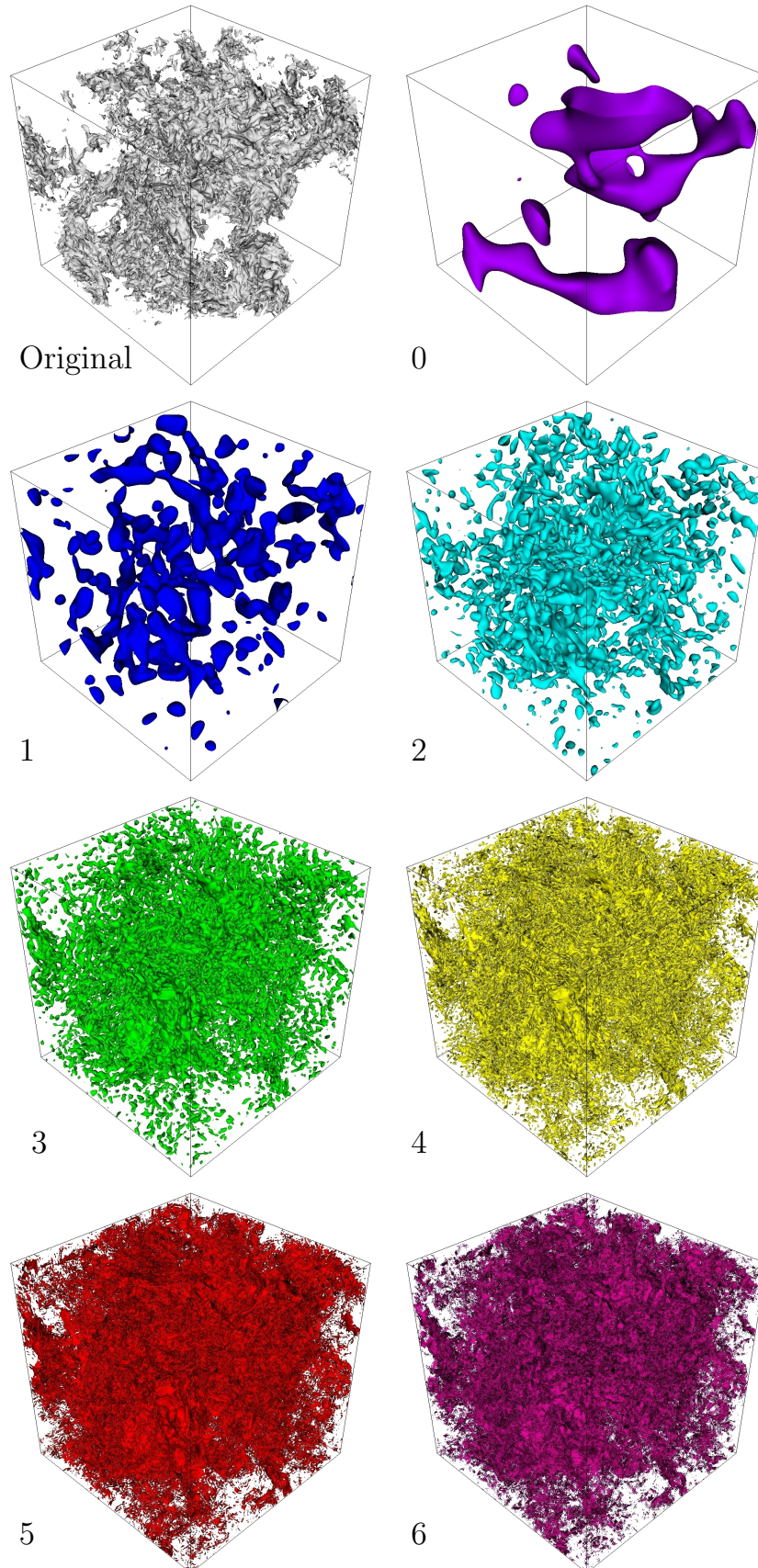
Figure 4.4: Iso-contours of the passive scalar fluctuation field for the original database (top left) and each one of the filtered scales resulting from the multi-scale analysis (filtering in the curvelet domain) (increasing scale number from left to right and top to bottom). A contour value equal to the mean plus two times the standard deviation of each resulting scalar field was used

go from predominantly blob-like and tube-like at scales 1–3 toward more sheet-like structures at the smaller scales 4 and 5, The stretching of the structures increases with the scale number; that is, the parameter λ decreases for smaller and smaller scales.

Some representative structures, named A–L, have been selected (see top of Figure 4.5); their corresponding signatures are shown in Figure 4.7. The cascade in the passive scalar fluctuation spectrum is thus translated into a cascade of the representation of structures in the visualization space, that starts near the point $(1, 1, 1)$ (sphere) and evolves toward highly stretched sheet-like structures. whose geometry tends to be complex (see, for example, their corresponding signatures in the last few points in Figure 4.7).

The clustering algorithm is then applied to the structures. The set of parameters $\{\hat{S}, \hat{C}, \lambda, d_l^S, d_u^S, d_l^C, d_u^C\}$ is used to form the feature space where each structure is represented by a point. Three groups of structures are obtained, and the result can be seen in Figure 4.8. That figure shows a visualization space with the same three spatial coordinates as in earlier plots (S, C, λ), and the structures represented by glyphs consisting of spheres (colored by the cluster ID and with radius scaled by the silhouette coefficient, defined in §2.3.3, that indicates the level of membership to the cluster to which it has been assigned) and horizontal bars with origin at the center of the sphere and lengths proportional to the other four parameters used for clustering (distances d_u and d_l in $\pm S$ and $\pm C$ directions). The thickness of these bars is also scaled by the value of the silhouette coefficient. Although the clustering algorithm captures the main trends, the structure geometries appear continuously distributed across the main groups, rather than separated into well-differentiated groups. This translates into the distribution of points and glyphs representing structures in the feature and visualization spaces: in particular, glyphs associated with the educed structures are organized as a cloud in the visualization space, transitioning from one region to other regions. For example, a comparison of the clustering results for the passive scalar field (Figures 4.8) and the test case of modeled structures (Figure 3.1) previously presented in §3 clearly shows the difference between the continuously distributed geometries of the structures educed for the passive scalar field, and the well distinct groups of geometries found in the test case. As a result, for the case of the passive scalar,
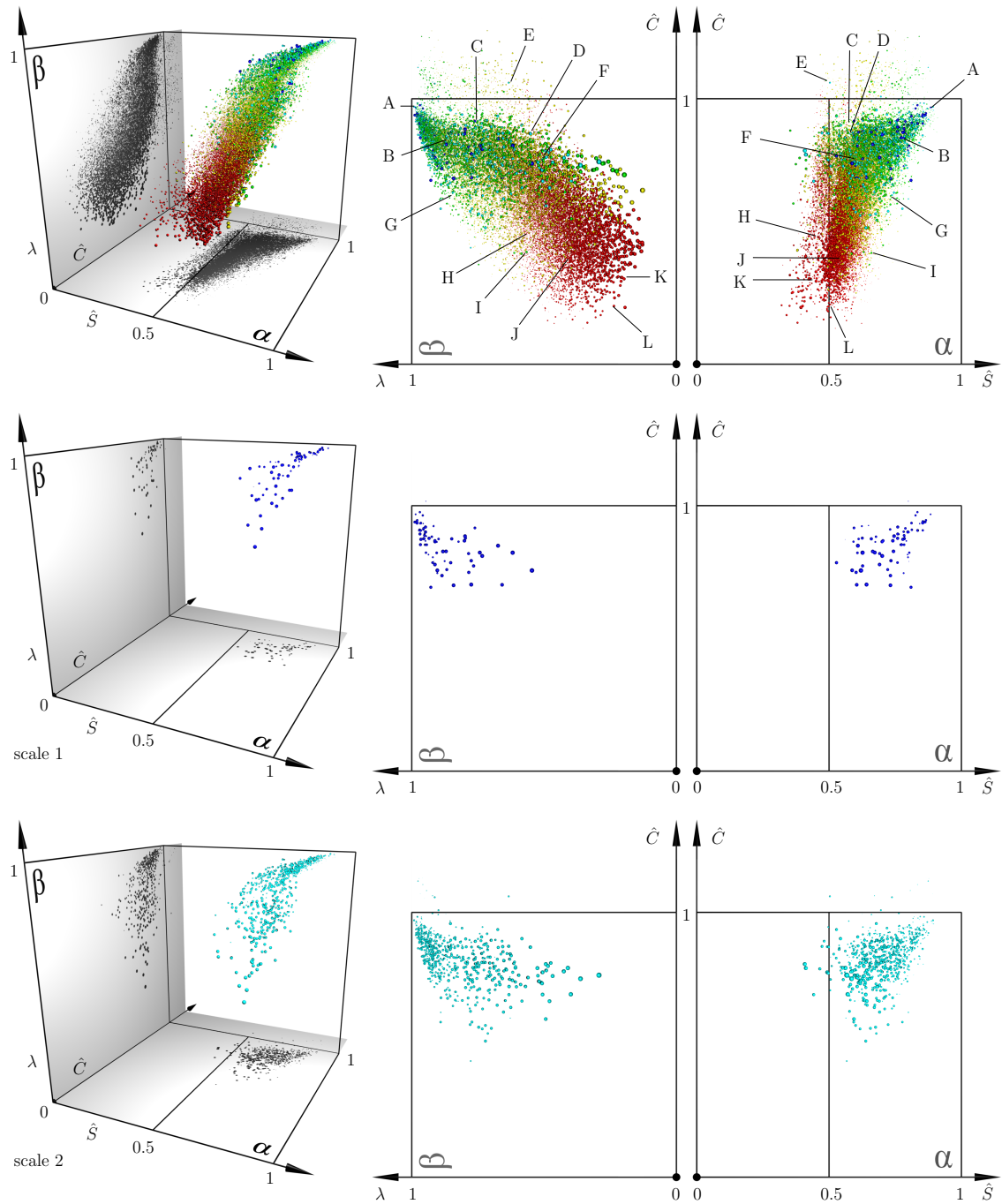
Figure 4.5: Visualization space with spheres representing the structures educed from the passive scalar fluctuation field at all scales (top), and only at scale 1 (middle) and 2 (bottom). Radii of spheres represents (in normalized logarithmic scale) the surface area of each structure. Color of the spheres represents the scale to which the structure belongs: dark blue (1), light blue (2), green (3), yellow (4), red (5). (Continued on Figure 4.6)
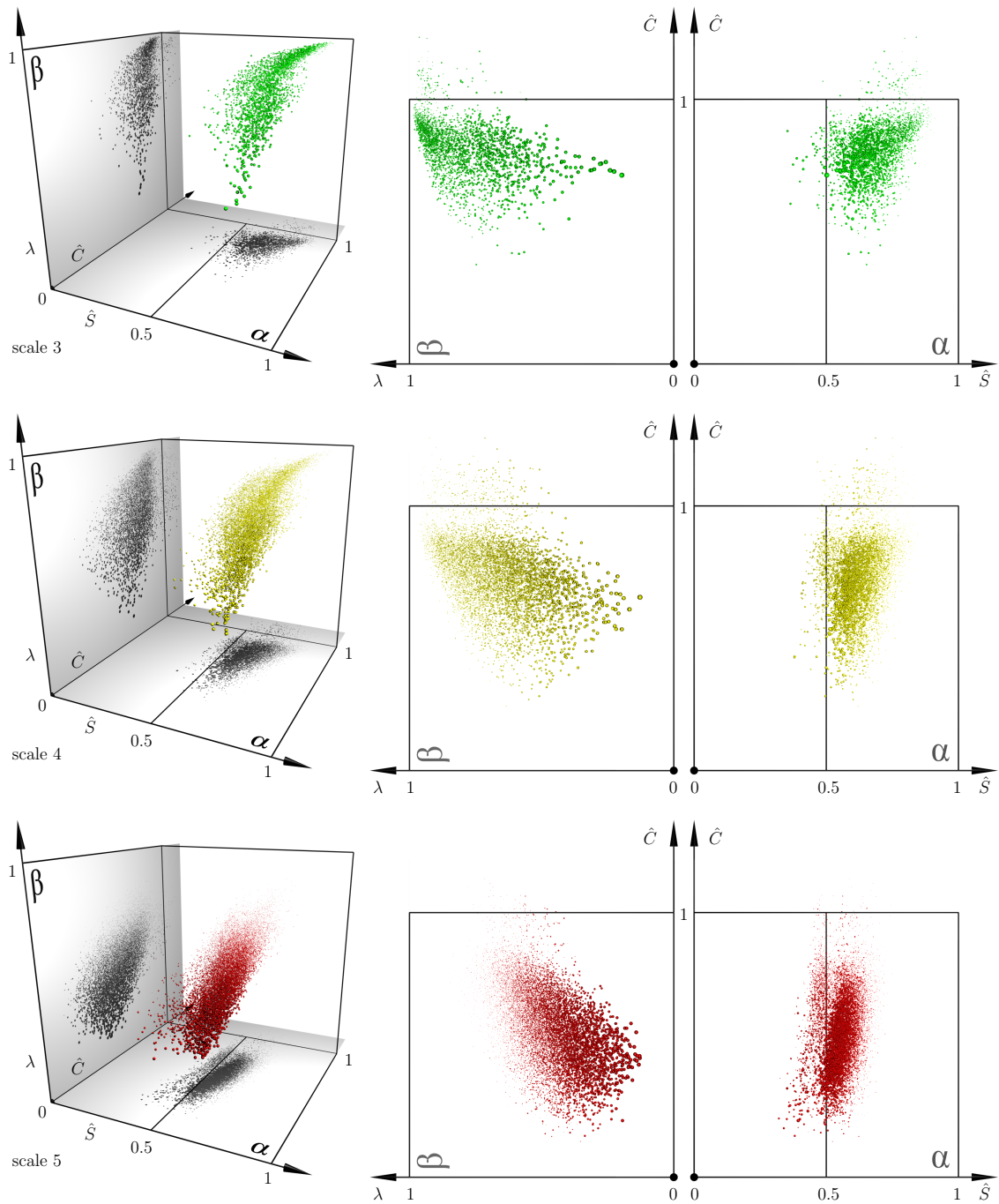
Figure 4.6: Visualization space with spheres representing the structures educed from the passive scalar fluctuation field at scale 3 (top), 4 (middle), and 5 (bottom). Radii of spheres represents (in normalized logarithmic scale) the surface area of each structure. Color of the spheres represents the scale to which the structure belongs: green (3), yellow (4), red (5). (Continued from Figure 4.5)
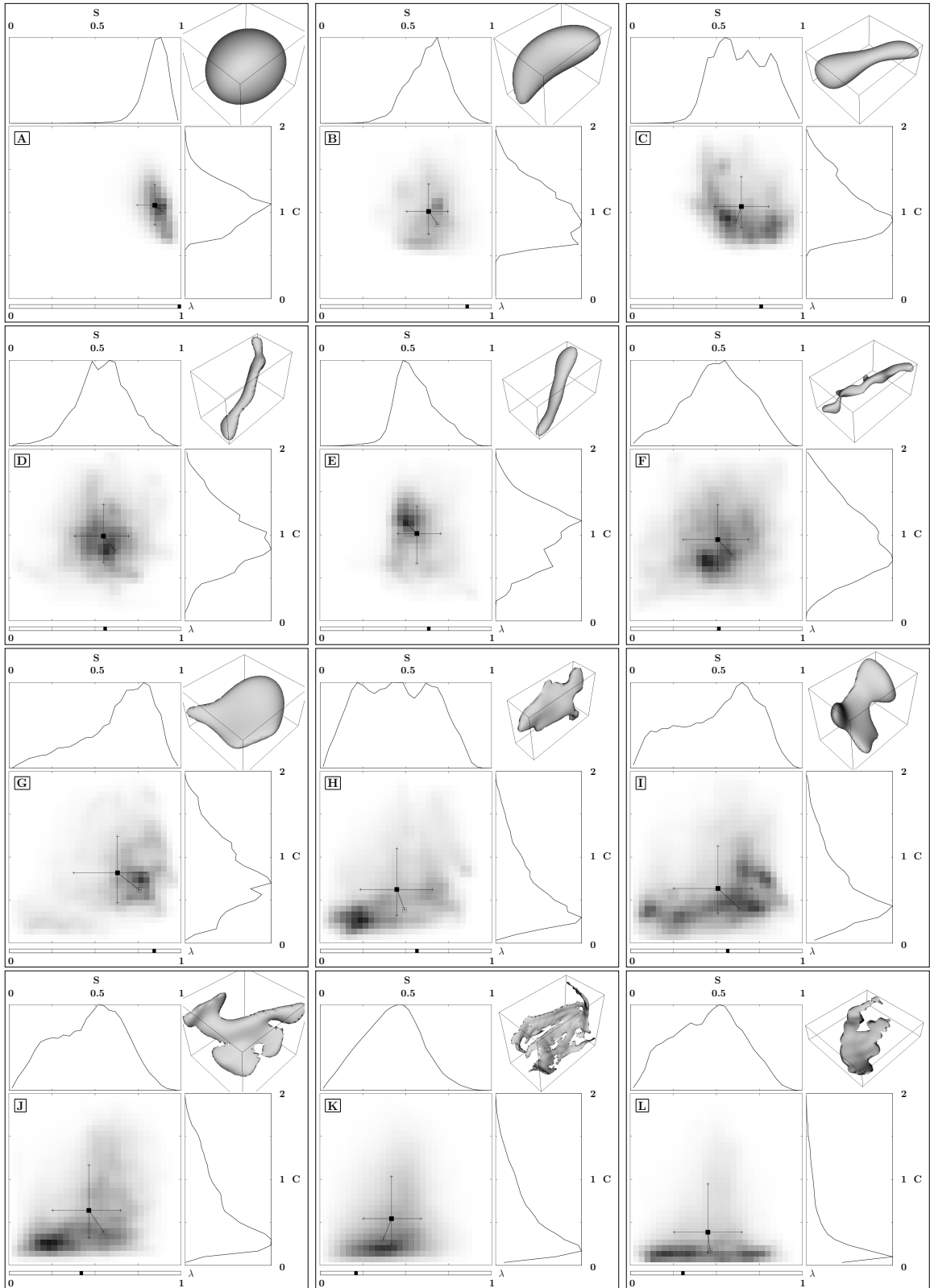
Figure 4.7: Signatures of representative structures (refer to Figure 4.5 (top) for the location of the corresponding points (A–L) in the visualization space)
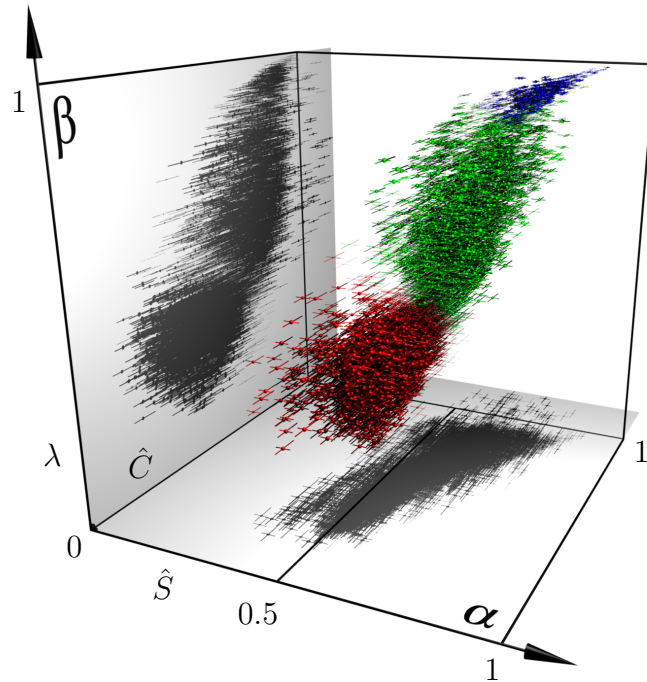
Figure 4.8: Result of the clustering algorithm in a visualization space showing spheres representing structures with radii scaled by the value of their silhouette coefficient (renormalized to have only positive values) and colored by the cluster to which they belong. An optimum number of three clusters was automatically found. The seven clustering parameters used to define the feature space are shown for each structure by the center of its representing sphere (of coordinates $\hat{S}, \hat{C}, \lambda$) and the four bars scaled by the value of d_u, d_l of S and C

some of the structures classified as belonging to one group but lying on the overlapping regions in the feature space will not necessarily be significantly different (geometrically) from other structures that belong to other groups but with a similar location in the feature space. The degree of membership to the educed clusters (measured by the silhouette coefficient) of those structures in the overlapping regions between clusters will therefore be lower than that of structures near the cluster centers. Note how the glyphs in Figure 4.8, scaled by the renormalized silhouette coefficient of the associated structures, are smaller in the overlapping regions (compare, for example, Figure 4.5 (top), where the density of points is much more continuous throughout the whole distribution, since the scaling factor in that case was the area of the structure, not its silhouette coefficient).

4.4   Discussion and physical interpretation

We discuss first the smallest scales. Figure 4.6 (bottom) shows that highly stretched sheet-like structures are predominant at those scales. From the size of the spheres representing the structures (related to the the surface area of the structures in a normalized logarithmic scale), we conclude that the larger of these structures appear more stretched (lower λ) and tend to be more sheet-like (lower $\hat{C}$). This trend is in agreement with the results of Schumacher & Sreenivasan (2005), who, using a conventional box-counting method, found that passive scalar iso-level sets at the smallest scales become smooth sheets. They did not find fractal structure in the passive scalar field within their range of Sc and Re_λ, which differ from present values. Schumacher & Sreenivasan also used the area-to-volume ratio of the iso-levels, which is essentially the parameter μ used in our methodology to form the dimensionless curvedness $\hat{C}$: they use this in a global sense rather than applied to individual structures, as is done here. In the study of intense strain structures in homogeneous isotropic turbulence by Moisy & Jiménez (2004), the dominance of sheet-like structures in the smallest scales, suggested by a similar box-counting method, was confirmed by the geometrical study of aspect ratios of individual structures.

Multi-scale decompositions of the vorticity field in turbulent flows have been previously applied using orthogonal wavelets in two and three dimensions (see Farge et al., 1999, 2001, 2003), where thresholding of the wavelet coefficients based on denoising theory separates the vorticity into two orthogonal fields, denoted as *coherent* and *incoherent* vorticity. It is found that the coherent field is responsible for most of the energy transfer in the large and inertial scales. In three-dimensional homogeneous isotropic turbulence, the pdf of the coherent vorticity is found to be stretched exponential while the incoherent vorticity is exponential. We find that the pdf of the scalar fluctuation (see Figure 4.3) is Gaussian, with sub-Gaussian tails, in agreement with previous results for scalar fields (Overholt & Pope, 1996; Celani et al., 2001). In our multi-scale decomposition (see Figure 4.3), the variance of the pdfs also decreases for smaller scales (resulting in narrower pdfs), quickly transitioning from Gaussian (with slightly sub-Gaussian tails) to exponential. Presently our multi-scale analysis does not include any assumptions about the 'coherence' of the educed structures through

thresholding of the multi-scale coefficients, since it has a different purpose, mainly as a diagnostics tool.

It has been suggested that exponential tails of the scalar fluctuation pdfs are linked to metrics of anomalous mixing (see the discussion in Warhaft (2000)). There have been attempts to clarify the conditions under which sub-Gaussian/exponential tails appear based on various factors that include relative simulation box size (Overholt & Pope, 1996; Schumacher & Sreenivasan, 2005), Reynolds number (distinguishing between 'soft' and 'hard' turbulence (Jayesh & Warhaft, 1992)), flow initial conditions and forcing (Jaberi et al., 1996), and, for the vorticity, the structure of intense portions of the field (Siggia, 1981; Kerr, 1985; Jiménez et al., 1993). The transition, seen in Figure 4.3, from Gaussian pdf in the larger scales to predominantly exponential pdfs in the smaller scales may be related to the geometry of individual structures present at each scale.

The presence of ramp-cliff structures in the scalar field (plateau–cliff in the scalar fluctuation) (Antonia et al., 1979) has been associated with anisotropy of the passive scalar field in the presence of a mean gradient (Celani et al., 2001; Overholt & Pope, 1996; Warhaft, 2000). These features are seen in the large scales (plateau regions) as well as in the small scales (cliffs of fronts), where steep changes in the values of the passive scalar occur (see Figure 4.2). The highly stretched, sheet-like structures found here at the smaller scales could be related to these fronts. A study of their spatial distribution with respect to proximity to the structures of the larger scales would be needed to confirm this. Further, the predominant orientation of the sheet-like regions of such structures could help to clarify their role. This could be obtained within the framework of the present methodology using the multi-orientation decomposition of the curvelet transform (not applied in this thesis).

For the present Sc and Re we know of no previous reports of blob- and tube-like (with moderate stretching) structures in the intermediate scales of the passive scalar fluctuation field. Theoretical developments in physical models of passive scalar mixing have utilized tube-like structures, stretched by large-scale strain fields, to analyze cascade and dissipation dynamics for a passive scalar (Pullin & Lundgren, 2001). Small-scale scalar mixing is modeled as a two-dimensional blob (a tube in three dimensions) convecting, deforming, and diffusing in the presence of the swirling motion of

a stretched spiral vortex. The blob is drawn out into rolled-up sheets whose azimuthally averaged structure remains tube-like. Within this compound tube-sheet structure, the derived scalar spectrum comprises two parts in the form of Batchelor (1959) k^{-1} and Obukov-Corrsin $k^{-5/3}$ (see Tennekes & Lumley (1974)) components. The $k^{-5/3}$ contribution arises from the non-axisymmetric scalar field which tends to be sheet-like. This dynamical model is not inconsistent with the present findings of tube and sheet structures at the smallest scales. We can hypothesize that blob-like structures, similar to structure A shown in Figure 4.7, are created first. These are then strained and stretched by the action of vortex tubes (D, E, F) to form vortex sheets (J, K, L). Further vortex tubes are then created by rolling-up of the sheets. Additional support for the validity of this picture as a physical mechanism of the cascade would probably require (at least) local correlation in tube and sheet structure locations and perhaps orientations for adjacent scales in the sense of the curvelet transform. Some of these topics will be covered in Chapter 7.